Synthetic eddy generation and modelling of turbine operation in a turbulent tidal flow

Matteo Gregori, Francesco Salvatore, Danilo Calcagni, and Roberto Camussi

Abstract—**This paper presents an original computational methodology to simulate the operation of hydrokinetic turbines in turbulent onset flows. Turbulent eddies are generated in the flow by volume forcing terms in the Navier–Stokes equations, and the intensity of the resulting turbulent stream is controlled to match prescribed conditions. The Navier–Stokes equations are numerically solved by a hybrid viscous/inviscid formulation in which a Boundary Integral Equation Method (BIEM) is used to predict the perturbation induced by a turbine, whereas the surrounding viscous flow is described by Detached Eddy Simulation (DES). The methodology is applied to simulate the operation of a horizontal–axis turbine in a 16% turbulent onset flow. The numerical results show that a divergence–free, nearly isotropic turbulent flow is established with a turbulence intensity 19% lower than the imposed value. Turbine loads are evaluated to quantify the effects of incoming eddies on device performance. By taking into account the velocity defect induced by the turbulence generation forcing terms, mean thrust and power coefficients are very close to those calculated in zero turbulence conditions, whereas fluctuations between 15% and 25% of the corresponding values in zero turbulence conditions are observed.**

Index Terms—**Tidal energy, turbulence, Synthetic eddy generation, DES, BIEM, Volume force method**

I. Introduction

THE performance and reliability of hydrokinetic turbines operating in marine sites and rivers is strongly affected by turbulence in the onset flow. Eddies with a wide range of spatial and time scales are primarily generated by surface winds and waves, shear layers in the water column, submerged obstacles. The entrainment of eddies into the rotor streamtube determines unsteady flow conditions on blades that result into transient forces and moments at blade root as well as fluctuating rotor thrust and power [1], [2].

The characterization of turbulence–induced loads is fundamental to design blades and powertrain components for enhanced fatigue–life performance in real operating conditions. To face the problem, the complex phenomenology of tidal stream turbulence is the subject of experimental campaigns in field sites, see *e.g.*, [3]–[5]. Real conditions are partially reproduced at laboratory scale in flume and towing tanks where the effect of turbulence on model turbine performance can be studied in controlled conditions [6], [7].

Complementary to experimental techniques, Computational Fluid Dynamics (CFD) is widely applied to investigate harmful operating conditions and to inform the design of enduring devices with no need of expensive component oversizing. A variety of approaches exists for the generation of a turbulent stream in the computational modelling of the fluid dynamic interaction between a solid body and the surrounding flow [8]. A broad classification distinguishes between precursor methods and synthetic methods. Precursor Methods (PM) are based on the assumption that turbulence can be injected into a computational domain by imposing as inlet condition a velocity distribution that describes a fully developed turbulent field. The input velocity distribution can be derived from experimental data or generated by an independent computational analysis [9], [10]. Synthetic Methods (SM) exploit a direct application of the classical Reynolds decomposition, where a turbulent flow is represented as the superposition of a baseline laminar flow and a randomly fluctuating velocity field [11], [12]. The latter can be generated as a noise function defined as the convolution between a random signal and a suitable filtering function, or by projecting the random velocity distribution onto a basis of harmonic functions [13]. Both PM and SM models have in common that the baseline flow is combined with an independent velocity perturbation that is injected to the flow (PM approach) or superimposed to it (SM approach). Once the resulting turbulent flow is established, its consistency with the solution of the Navier-Stokes equations remains to be demonstrated. Dealing with incompressible flows, further modelling is often required to enforce the divergence–free condition is satisfied [14]. A particular case of Synthetic Methods is the Synthetic Volume Forcing Methods (SVFM). The idea is to generate turbulent structures in an arbitrary flow by introducing obstacles in the computational domain that are simulated by volume forcing terms in the right–hand side of the Navier-Stokes equations. In this case, the turbulent onset flow is generated as part of the CFD problem. Examples are *e.g.*, [15], [16], for aerodynamics studies, and [17] dealing with tidal turbine flow simulations.

This work was supported in part by the ULYSSES 2030 Project by CNR (DIT.AD019.118).

Matteo Gregori was with the Institute of Marine Engineering of the National Research Council of Italy, Via di Vallerano 139, 00128 Rome, Italy. He is now at Rina Consulting SpA (e-mail: matteo.gregori@rina.org).

Francesco Salvatore is with the Institute of Marine Engineering of the National Research Council of Italy, Via di Vallerano 139, 00128 Rome, Italy (e-mail: francesco.salvatore@cnr.it).

Danilo Calcagni is with the Institute of Marine Engineering of the National Research Council of Italy, Via di Vallerano 139, 00128 Rome, Italy (e-mail: danilo.calcagni@cnr.it).

Roberto Camussi is at Roma Tre University, Department of Engineering, Via della Vasca Navale 79, 00146 Rome, Italy (e-mail: roberto.camussi@uniroma3.it).

Digital Object Identifier:
https://doi.org/10.36688/ewtec-2023-307

The present work deals with a SVFM approach based on an original definition of the forcing terms used to generate turbulent structures in the baseline flow. The volume force terms are defined by a random distribution combined with a superposition of sinusoidal harmonics with random phase. The distribution is imposed in a thin layer in the upstream part of the computational domain. The requirement to reproduce a turbulent flow with given properties is obtained by tuning the intensity of the volume force distribution by a Proportional-Integral-Derivative (PID) control strategy. The variance of the flow velocity components are used as control variables. In [18] the model was initially applied to describe a turbulent stream in an unbounded flow studied by Detached Eddy Simulation (DES). The capability to generate eddies that evolve into a homogeneous, isotropic turbulent flow with given intensity was discussed.

The methodology proposed in [18] is extended here to analyze the interaction between the generated onset turbulent flow and a tidal turbine. By DES, the turbine can be described as a solid obstacle with suitable treatment of the no-slip condition at walls. An alternative computationally efficient approach is used in which the turbine is simulated by a volume force method, in a similar fashion as turbulence generation is modelled. Specifically, a hybrid viscous/inviscid flow methodology is applied in which the DES solver is strongly coupled with a Boundary Integral Equation Method (BIEM) solver for inviscid flows. At each time step, the blade load distribution is calculated by a time-accurate BIEM solution and recast as volume force terms that are plugged into the DES solution. Both DES and BIEM solvers are in–house built at the Institute of Marine Engineering of the Italian National Research Council (CNR-INM) and have been extensively validated for marine propulsors and tidal turbines [19]–[21].

The numerical application deals with a 3-bladed horizontal-axis tidal turbine in a 16% intensity turbulent onset flow. The methodology is described in sections II and III, details of the case study and of the computational set–up are given in section IV, whereas numerical results are presented and discussed in section V. Particular attention is given to characterize the generated turbulent stream in terms of key metric quantities like turbulence intensity, Power Spectral Density (PSD), time and spatial means, isotropy. The numerical results are discussed to assess the capability of the proposed methodology to provide a physically-consistent description of the operation of a tidal turbine in a real turbulent flow.

II. Formulation for viscous flows with turbulence generation

A general formulation for turbulent viscous flows is given by the Navier-Stokes equations where the classical Reynolds decomposition is used to represent the velocity field $\mathbf{u} = \mathbf{u}(\mathbf{x}, t)$ and the pressure field $p = p(\mathbf{x}, t)$ as the combination of mean and randomly fluctuating terms

$$\mathbf{u} = \overline{\mathbf{u}} + \mathbf{u}'; \qquad p = \overline{p} + p', \tag{1}$$

where the overbar symbol denotes a mean quantity and, by definition, $\overline{\mathbf{u}'} = \overline{p'} = 0$.

Consider a 3D Cartesian orthogonal frame of reference $(Ox_1x_2x_3)$ with unit vectors $\mathbf{e}_i (i = 1, 2, 3)$. Under incompressible flow assumptions, mass and momentum equations for mean variables can be written as (hereafter the overbar symbol for mean quantities is omitted)

$$\begin{aligned} &\frac{\partial u_i}{\partial x_i} = 0 \qquad (i = 1, 2, 3) \\ &\frac{\partial u_i}{\partial t} + u_j \frac{\partial u_i}{\partial x_j} = -\frac{\partial p}{\partial x_i} + \frac{\partial}{\partial x_j} T_{ij} + f_i \end{aligned} \tag{2}$$

where repeated indices denote summation. The quantity T_{ij} describes the components of the Reynolds stress tensor $\mathbf{T} = (u_i' u_j')\mathbf{e}_j\mathbf{e}_i$ that, under the Boussinesque turbulent viscosity assumption, read

$$T_{ij} = \frac{1}{Re_{_T}} \left(\frac{\partial u_i}{\partial x_j} + \frac{\partial u_j}{\partial x_i} \right) \tag{3}$$

where $Re_{_T}$ is the Reynolds number referred to the turbulent viscosity $\mu_{_T}$.

In the right-hand side of Eq. (2), the quantity $f_i = \mathbf{f} \cdot \mathbf{e}_i$ denotes the i–th component of a generic volume force field. In the present formulation, a volume–force approach is used to define forcing terms in the momentum equation that are responsible for perturbations to the onset flow. This includes a contribution $\mathbf{f}_{_B}$ to represent the perturbation induced by a turbine, as it will be discussed in section III. Similarly, a volume–force distribution $\mathbf{f}_{_T}$ is defined to inject turbulent eddies in the flow. Assuming no other volume force distributions exist, one has

$$\mathbf{f} = \mathbf{f}_{_T} + \mathbf{f}_{_B} \tag{4}$$

A. Volume force generation model

The proposed approach to generate turbulence in an arbitrary onset flow falls within the class of Synthetic Volume Forcing Methods (SVFM). A review on SVFM formulations and the detailed derivation of the present model are given in [18], whereas the methodology is briefly recalled here. The underlying assumption common to all SVFM formulations is that volume forcing terms in the right–hand side of the momentum equations (2) can be used to simulate the presence of an obstacle in the flow whose effect is to generate a turbulent wake downstream of it. The physical interpretation is found in the grids that are used in wind tunnels and water flumes to generate a requested turbulence level in the test section [22]. The definition of the volume force distribution characterizes the properties of the turbulent stream that can be generated.

In the present approach, the forcing terms are defined as a spatially random distribution combined with a superposition of sinusoidal harmonics with random phase. Assuming the unperturbed onset flow is uniform and aligned to the x_1 axis, the distribution $\mathbf{f}_{_T} = \mathbf{f}_{_T}(\mathbf{x}, t)$ is zero throughout the computational domain except for a small region conveniently located upstream of the region of interest, *e.g.*, where a turbine is located. This *generation* region consists in a thin layer

in the x_1 direction and covers a wide area in the normal direction. The Cartesian components of the baseline volume force distribution $\mathbf{f}_{T,0}$ are defined as follows

$$\begin{aligned}(f_{T,0})_i(\mathbf{x},t) &= C_1 \sum_{k=1,N_k} [\sin(2\pi\lambda_k x_2 + \psi'(t)) \\ &+ \sin(2\pi\lambda_k x_3 + \psi''(t))] \\ &+ C_2\, W(x_2,x_3,t) \qquad (i=1,2,3)\end{aligned} \tag{5}$$

where N_k is the number of harmonic terms and λ_k is the wavelength associated to each term. The phases ψ' and ψ'' and the quantity W are built from a constant probability density function that generates pseudo random values in the range $[0:1]$. Quantities ψ' and ψ'' are further scaled to fit in the $[-\pi:\pi]$ range. By definition, W values at distinct points $\mathbf{x}_a, \mathbf{x}_b$ or time instants t_1, t_2, have zero correlation. Finally, the constants C_1, C_2 are used to normalise the baseline volume force intensity in the range $[-1:1]$. An example of random volume force distribution obtained by Eq. (5) with $N_k = 1$ is shown in Fig. 1, taken from [18].

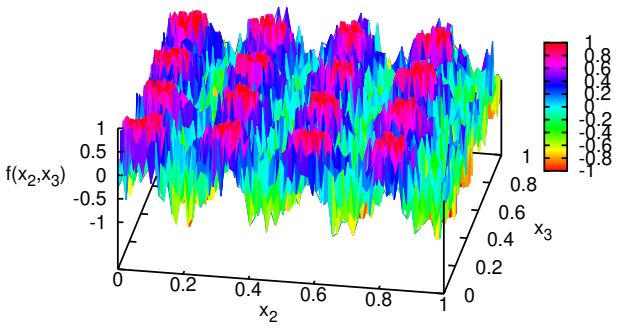

Fig. 1. Sample of the baseline random distribution of volume forces from Eq. (5) ($N_k = 1$, and λ_1 equal to 1/4 of span).

B. Turbulence metrics and control strategy

The baseline volume force distribution defined by Eq. (5) is general and can be used to generate eddies with arbitrary intensity by varying the C_1, C_2 constants. Further modelling is required in order to obtain that the perturbation to the flow corresponds to an expected amount of turbulence downstream of the generation region. This aspects is of primary importance in the attempt to simulate the conditions in a real tidal site with a specific turbulent flow climate.

The characterization of perturbed flow conditions is achieved by evaluating the statistical properties of the velocity field. A review on turbulent flow metrics can be found *e.g.*, in [23]. By following a classical approach for the analysis of random phenomena, the correlation between fluctuating velocity components is introduced to derive key metric quantities. Denoting by $\mathbf{r} = \mathbf{x} - \mathbf{x}_0$ a position vector with respect to an arbitrary point $\mathbf{x}_0$, the spatial correlation tensor reads

$$R_{ij}(\mathbf{r}) = E\left[u_i'(\mathbf{x})\, u_j'(\mathbf{x}+\mathbf{r})\right] \tag{6}$$

where the symbol $E[\,]$ denotes the expected value operator. A dual definition holds for the time correlation tensor as $R_{ij}(\tau) = E[u_i'(t)\, u_j'(t+\tau)]$, where τ is an arbitrary time. For $\mathbf{r} = 0$ or $\tau = 0$, the quantity $R_{ij}(0)$ equals the Reynolds stress tensor, and each diagonal term defines the flow variance σ_i^2 in the x_i direction. A common definition of the turbulent intensity I_∞ is

$$I_\infty = \frac{1}{u_\infty}\sqrt{\frac{1}{3}\sum_{i=1}^{3}\sigma_i^2} \tag{7}$$

where u_∞ is a reference mean flow speed. Under homogeneous isotropic turbulence assumptions, one has $\sigma_1^2 = \sigma_2^2 = \sigma_3^2$, and by introducing $\sigma^2 = \sigma_i^2\ (i=1,2,3)$, Eq. (7) yields $I_\infty = \sqrt{\sigma^2}/u_\infty$.

The problem of simulating given turbulent flow conditions by Eq. (5) can be formulated as tuning the volume force distribution so that the generated flow has the requested intensity I_∞ or variance terms σ_i^2. In order to accomplish this, a control strategy is implemented to dynamically modify the spatial and time distribution of volume force terms in Eq. (5). Specifically, a standard Proportional-Integral-Derivative (PID) controller is applied, and variance terms σ_i^2 in the flow downstream of the turbulence generation region are observed by the control algorithm. Assuming the target condition is to establish homogeneous and isotropic turbulence with a given variance intensity σ_{des}^2, the deviation between generated and target conditions can be described through the following error functions $\mathcal{E}_i, (i=1,2,3)$

$$\mathcal{E}_i = \left(\sigma_{des}^2 - \sigma_i^2\right)/\sigma_{des}^2 \tag{8}$$

The minimization of the error functions above is obtained by the PID control through the parameters $k_i, (i=1,2,3)$ defined as

$$k_i(t) = a_{1\,i}\mathcal{E}_i(t) + a_{2\,i}\int_{t_0}^{t}\mathcal{E}_i(t)dt + a_{3\,i}\frac{\partial}{\partial t}\mathcal{E}_i(t) \tag{9}$$

where $t_0 < t$, and the coefficients $a_{1\,i}, a_{2\,i}, a_{3\,i}$ define, respectively, the proportional, integral and derivative control parameters for the i–th component.

Quantities $k_i(t)$ are used as tuning functions for the baseline volume force distribution, and Eq. (5) is recast as $(i=1,2,3)$

$$(f_T)_i(\mathbf{x},t) = k_i(t)\,(f_{T,0})_i(\mathbf{x},t) \tag{10}$$

III. Instream turbine model

The turbulence generation and control model described in the previous section can be combined with an arbitrary formulation for the numerical solution of the Navier-Stokes equations for turbulent viscous flows. In the present work, a hybrid viscous/inviscid flow model is applied to study the interaction between a horizontal axis turbine and the incoming flow. The methodology is briefly described here, whereas details are given in [24], with applications to an isolated turbine and to two in-line turbines.

The approach consists in the coupling between an inviscid–flow model that predicts the perturbation induced by the turbine and a viscous–flow model that describes the turbulent flow in which the turbine is immersed. The turbine simulation is performed

by a Boundary Integral Equation Model for inviscid flows (BIEM, [20]), whereas the turbulent viscous flow around the turbine is described by a numerical solution of the Navier-Stokes equations by Detached Eddy Simulation (DES, [25]). The coupling between viscous and inviscid-flow solutions is established by a volume–force/effective–inflow iterative approach. Each step of the iteration corresponds to a physical time step of the time marching solution for both BIEM and DES solvers. In the BIEM solution, the impermeability condition on the turbine surface is imposed by considering the incoming flow calculated by DES by removing the turbine–induced velocity calculated under inviscid flow assumptions (effective inflow). The hydrodynamic forces on turbine blades calculated by BIEM are recast as volume forces $\mathbf{f}_B$ in Eqs. (4) and (2). To ensure a time–accurate representation, the volume forces are distributed in volume grid cells corresponding to the actual position of blades at each time step. The DES solution including the turbine–induced forcing terms is used to update the flow incoming to the turbine for the BIEM solution at the next time step and the procedure is repeated, as sketched in Fig. 2.

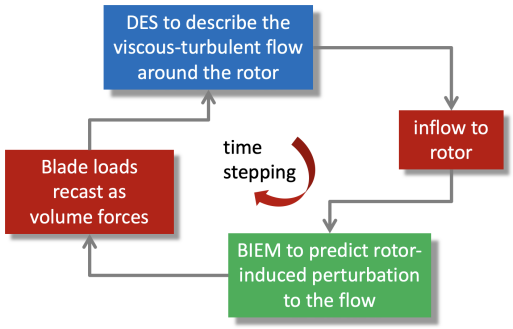

Fig. 2. Iterative procedure for the hybrid DES/BIEM solution.

Both BIEM and DES solvers are in–house built at CNR-INM. The BIEM solver is valid for unsteady flows around lifting bodies in arbitrary motion with respect to a uniform or non–uniform incoming flow. Under inviscid, irrotational flow assumptions, Eqs. (2) are recast as the Laplace equation for the velocity potential $\varphi = \nabla \mathbf{u}$, and the Bernoulli equation for the pressure [26]. A trailing wake model is introduced to describe the mechanism of generation of vorticity and the associated lift and induced drag forces on turbine blades. A simple Viscous Flow Correction (VFC) model allows to estimate the effect of viscosity on blade loads that is neglected by the inviscid flow condition. The correction is obtained by comparing lift and drag forces calculated at each blade section by BIEM with the corresponding viscous forces on 2D foils having the same geometry of blade sections and operating at the same conditions in terms of velocity and angle of attack, where three–dimensional flow effects are predicted by BIEM. The X-Foil solver [27] is used to determine 2D viscous flow lift and drag curves.

The DES solver is part of a general purpose Navier–Stokes code based on a finite volume technique with pressure and velocity co–located at cell center. Viscous terms are integrated by a standard second order centered scheme, whereas for the convective and pressure terms a third order upwind scheme is chosen. A library of turbulence and Large Eddy Simulation (LES) models is available, whereas Detached Eddy Simulation is based on the Spalart–Allmaras turbulence model [28]. Under incompressible flow conditions, at every time step a divergence–free velocity field is enforced by an artificial compressibility approach, in which a pseudo–time derivative is introduced in the discretized system of equations [29]. The solver is written for a structured volume mesh with partially overlapping blocks that are processed by a chimera algorithm to interpolate the solution among different sub–grids [19].

It is worth to observe that combining the turbulence generation model in section II and the hybrid viscous/inviscid turbine flow model, a unified volume–force methodology is obtained. In particular, the volume force distributions $\mathbf{f}_B$ and $\mathbf{f}_T$ in Eq. (4) are independent in that the mechanism of production is different and the flow regions where they are distributed are completely disjoint.

IV. Numerical application

The generation of a homogeneous isotropic turbulent flow by the volume force model in section II was presented in [18] for the particular case of an unbounded flow. In this section, the extension of the methodology to the analysis of a tidal turbine in the generated turbulent flow is addressed.

The case study is a three–bladed horizontal–axis turbine operating at constant rotational speed n (rps) in a uniform onset flow with turbulence intensity $I_\infty = 0.16$ and averaged speed $V_0 = 2.0$ m/s. Assuming a design TSR $\lambda = 5$, this yields a turbine rotational speed $n = 6.38$ rps. Main turbine geometry data are given in Table I and describe a commercial design by Schottel Hydro [30]. At model scale, this turbine has been extensively studied by flume tank tests, see *e.g.*, [31].

TABLE I
Model turbine geometry parameters.

Rotor diameter (model scale), D	0.5 [m]
Blades number, Z	3
Pitch angle at 70% span, Φ_{07}	7.5 [deg]
Pitch angle at tip, Φ_{tip}	5.3 [deg]
Thickness ratio, 70% span, t/c	0.125 [-]
Hub/rotor diameter ratio	0.09 [-]
Blade section profile	Schottel Hydro

The numerical solution describing the turbine in the turbulent onset flow is obtained by a code in which the DES and BIEM solvers are strongly coupled, as described in section III. For the sake of clarity, the computational set-up for the DES and BIEM parts are separately described.

A. Computational set-up: DES and turbulence generation

The computational domain for the numerical solution by DES is a flow region delimited by a cylinder with axis aligned with the x_1 axis and parallel to the direction of the unperturbed flow, Fig. 3.

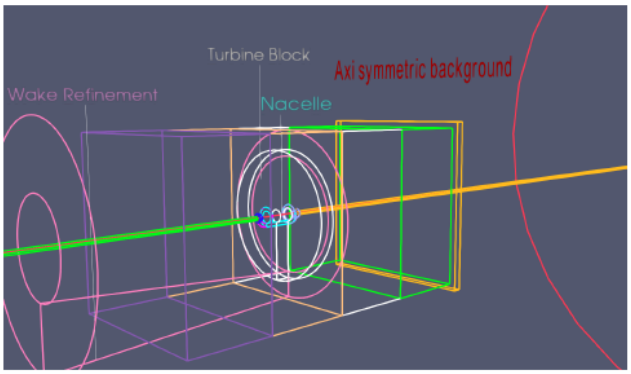

Fig. 3. Volume grid for the DES solution.

With reference to the turbine diameter D, the cylinder has diameter $9D$, length $26D$, with the upstream base (inlet section) at $x_1 = -15D$, and the downstream base (outlet section) at $x_1 = 11D$, with the turbine plane at $x_1 = 0$. An hexahedral grid block defines the region where the volume forces $\mathbf{f}_T$ are distributed and turbulence is generated (*generation* block). This block is placed one diameter upstream of the turbine plane, is $0.05D$ thick in the streamwise direction, and $1.4D \times 1.4D$ wide in the crossflow directions. Downstream of it, an hexahedral grid block defines the flow region where the generated turbulence is monitored and statistical properties are evaluated (*control* block). This block is $2D$ long in the x_1 direction and $1.3D \times 1.3D$ wide. Recalling a hybrid DES/BIEM approach is used, the blades do not represent solid boundaries and a simple grid in the turbine region is built. Five body–fitted blocks discretize the flow region around the nacelle, with grid refinement in direction normal to the wall. A toroidal block delimiting the region swept by rotating blades delimits the domain where blade–induced volume forces $\mathbf{f}_B$ are distributed (*rotor* block). Downstream of it, a toroidal block is placed to refine the grid in the flow region where the tip vortices shed at blade tips are convected downstream. The computational domain is completed by a background block that is internally delimited by a thin cylindrical gap that is filled with two partially overlapping hexahedral blocks extended from the centre of the domain to the inlet and to the outlet sections. Dimensions and number of cells of main grid blocks are summarized in Table II. The number of cells is referred to the finest grid level, with coarser levels obtained by removing every other point from the finer one. For the present study, a 3 levels mesh was built, with a total of 13.4M cells in the finest level. A sketch of the discretization in the the near field region on the longitudinal plane $x_3 = 0$ is illustrated in Fig. 4.

Combining the volume force representation of blades, and the overlapping–grid technique in the DES solver, the generation of a structured multi–block mesh becomes a trivial task that in the present study has been performed by using an in–house developed, automated grid generation tool.

No–slip boundary conditions are enforced at the nacelle solid walls. At the inlet boundary the velocity is set to the undisturbed flow value, whereas at the outflow the pressure is set equal to zero.

TABLE II
VOLUME GRID: MAIN BLOCKS SIZE L_i IN THE i–WISE DIRECTION ($i = 1, 2, 3$), AND NUMBER OF CELLS IN THE FINEST LEVEL.

Block	L_1/D	L_2/D (r/D)	L_3/D	No. cells
Generation	0.05	1.4	1.4	$24 \times 120 \times 120$
Control	2.0	1.3	1.3	$320 \times 160 \times 160$
Nacelle	0.11	(0.05)	–	$160 \times 56 \times 96$
Rotor	0.1	(0.5)	–	$96 \times 240 \times 40$
Wake	1.5	(1.3–1.6)	–	$184 \times 240 \times 40$
Background	26.0	(9.0)	–	$200 \times 64 \times 96$

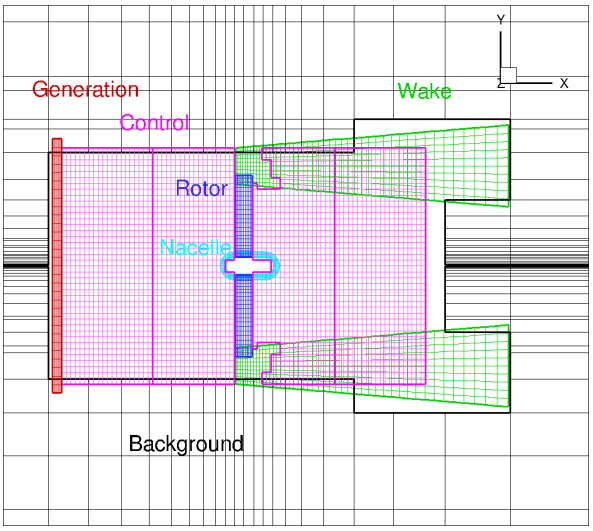

Fig. 4. Discretized near field region in the longitudinal plane $x_3 = 0$. The coarsest grid level is represented.

B. Computational set-up: BIEM model

The BIEM solution requires the discretization of the turbine surface (blades and nacelle) and of the helicoidal wakes shed at each blade trailing edge. Figure 5 shows details of the mesh, whereas the size of each grid patch is given in Table III. Similarly to the volume grid discussed above, the surface mesh has been automatically generated from the turbine 3D model by an in–house developed tool.

TABLE III
MODEL TURBINE: BIEM GRID DISCRETIZATION ELEMENTS.

Blade	36 (chordwise)	30 (spanwise)
Hub	72 (axial)	30 (peripheral)
Wake	90 (streamwise)	30 (radial)

C. DES/BIEM coupling

The solution of the coupled DES/BIEM problem is obtained by a time–marching calculation. At each physical time step, a pseudo–time cycle is performed to enforce the divergence–free condition of the velocity field in the DES solver. Within the pseudo–time loop, calls to the BIEM solver are repeated to achieve convergence of the flow perturbation induced by the volume forces $\mathbf{f}_B$ representing blade loads. The evaluation of volume forces $\mathbf{f}_T$ to inject turbulence in the onset flow is repeated at each step of the physical time loop.

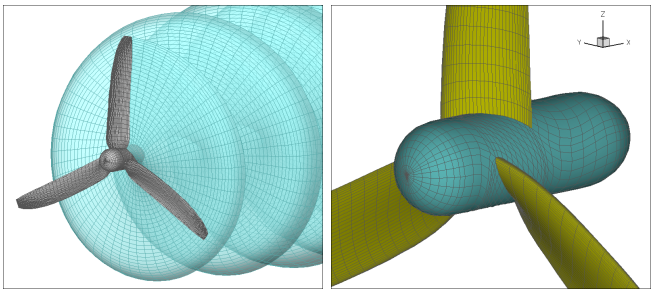

Fig. 5. Computational grid for the BIEM solution of the turbine flow. Left: full turbine assembly and trailing wake shed by one blade. Right: detail of the nacelle and blade roots.

The physical time step used in the present study is $\Delta t = 0.001309s$. Considering the nominal inflow velocity and the computational grid dimensions, the perturbation originated at the generation block takes about 2300 steps to be convected to the outlet of the computational domain. At TSR 5, the rotation of the turbine at each time step is 3.0 degrees, and DES and BIEM time–marching solutions are sinchronized. As example, Fig. 6 shows the residuals of the DES solver during 5 physical time steps, corresponding to about 150 pseudo–time steps in total. Within the pseudo–time cycle, the residuals of the velocity components reach values below 10^{-3} whereas pressure residuals drop to $2{\cdot}10^{-3}$.

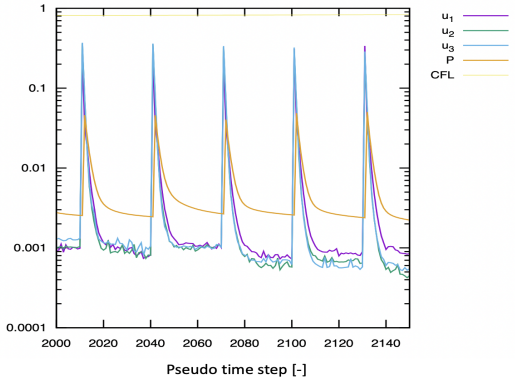

Fig. 6. Velocity and pressure residuals of DES solver in the coupled DES/BIEM solution during 5 pseudo–time cycles.

V. Results and Discussion

The computational analysis combining the hybrid DES/BIEM model, and the volume force turbulence generation model has been performed with the main objective to characterize turbine loads and wakefield with a turbulent onset flow and to compare results with laminar uniform inflow conditions. A key aspect is the capability of the volume force model described in section II to generate a stationary homogeneous isotropic turbulent flow with a given intensity I_∞. Similarly, the capability of the coupled DES/BIEM solver to correctly determine the perturbation induced by the turbine to the surrounding flow has been investigated.

A. Turbine loads and induced flow by BIEM

The turbine performance is characterized in terms of thrust T, torque Q and power coefficients as

$$\begin{aligned} C_T &= \frac{T}{1/2\rho A V_\infty^2}, \\ C_Q &= \frac{Q}{1/2\rho A V_\infty^2 R}, \\ C_P &= \frac{Q\,\Omega}{1/2\rho A V_\infty^3} = C_Q \cdot \lambda \end{aligned} \tag{11}$$

where $R = D/2$ is the rotor radius, $A = \pi R^2$ is the swept area, and $\Omega = 2\pi n$ the angular velocity. The non-dimensional kinematic parameter λ denotes the Tip Speed Ratio (TSR)

$$\lambda = \frac{\Omega R}{V_\infty} \tag{12}$$

Figure 7 presents turbine thrust and power curves predicted by BIEM over a full range of operating conditions from deep stall to overspeed. Plotted data have been normalized with respect to measured C_T, C_P values at $\lambda = 5$ (design point). The numerical predictions include viscosity effects by the VFC model as described in Section III, and are compared with measurements performed at the CNR-INM depressurized flume tank by using a 500 mm diameter model [31] with a 2.0 m/s onset flow speed. Nominal turbulence in the flume tank is about 3%, which can be considered to have a negligible impact on turbine performance. The comparison with experimental data demonstrates that the BIEM model with viscous–flow correction provides reliable predictions of turbine hydrodynamic loads. In particular, both thrust and power are accurately predicted across the turbine operational range.

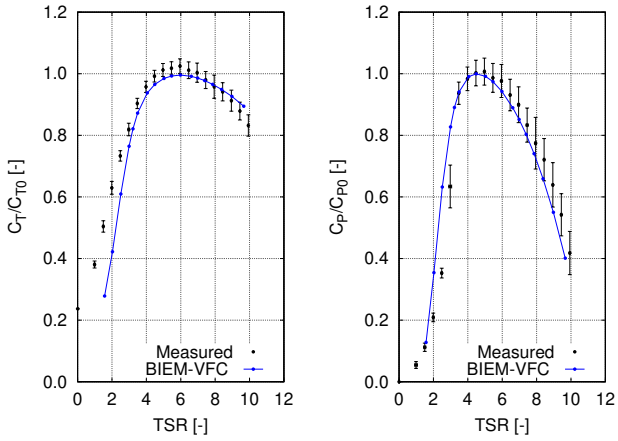

Fig. 7. Turbine performance curves by BIEM. Normalized coefficients of thrust (left), and power (right).

Turbine thrust and power values at each TSR are obtained by integrating normal stress (pressure) and tangential stress (friction, by the VFC model) over the surface of blades. A triaxial view of the turbine and the trailing wake shed by one blade is presented in Fig. 8. The contourmap depicts the distribution of the pressure coefficient $c_p = (p - p_0)/[1/2\rho(n\,D)^2]$, where p_0 is the ambient pressure.

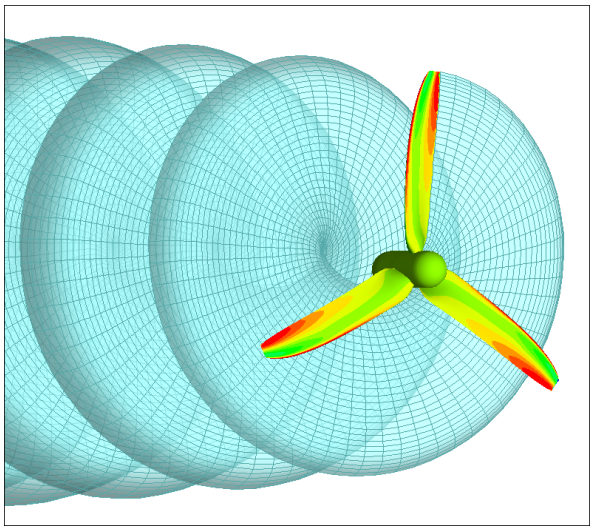

Fig. 8. Triaxial view of the turbine with trailing wake pattern and pressure coefficient distribution on blade surface by BIEM ($\lambda = 5$).

The surface load on each blade is averaged between suction and pressure sides to obtain mean load surface distributions. An example of non dimensional axial, tangential and radial components of mean surface loads at $\lambda = 5$ are plotted in Fig. 9. The volume force distribution $\mathbf{f}_B$ in eq. (4) is obtained by projecting mean surface loads on the rotor block of the volume grid in Fig. 3, by using the procedure described in [32]. Under non–uniform inflow conditions, different distributions from each blade are evaluated. This is the case in the present study, where incoming turbulent eddies determine a non–homogeneous inflow that results into transient blade loads. The calculated volume force distribution is time–accurate, as it preserves the actual position of rotating blades at each time step of the hybrid DES/BIEM solution.

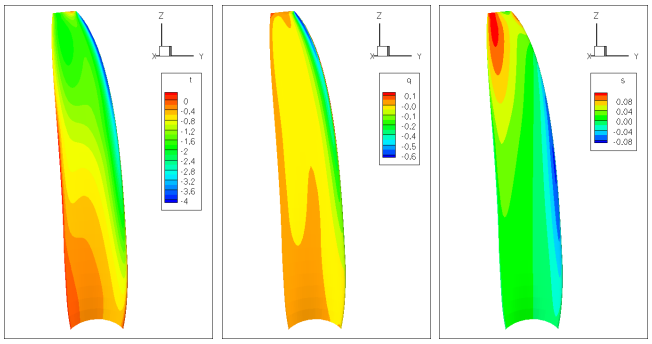

Fig. 9. Sample mean blade load distribution by BIEM. Left to right: axial, tangential, radial components ($\lambda = 5$).

B. Hybrid DES/BIEM study of zero turbulence conditions

The turbine blade loading by BIEM is used in the hybrid DES/BIEM model to determine the perturbation induced by the rotor to the surrounding flow. By plugging this pertubation into the DES solution, a physically–consistent description of the complex interplay between the vortical structures shed by turbine blades and the viscous flow can be obtained. In order to better analyze the impact of onset flow turbulence, the flowfield solution with no turbulence generation (zero infow turbulence) is presented first. The turbine operating condition at $\lambda = 5$ is considered. Assuming a kinematic viscosity $\nu = 1.004\,10^{-6}$ m^2/s, and recalling $V_0 = 2.0$ m/s, and $D = 0.5$ m, the reference Reynolds number is $Re = DV_0/\nu = 0.996\,10^6$.

Figure 10 presents the distribution of the axial velocity u_1 and of the vertical velocity u_3 in the longitudinal plane $x_2 = 0$ at a representative time step when the solution reaches a regime condition. The flow is directed left to right and velocity is non dimensional with respect to V_0. Recalling the turbine blades are represented by a volume force model in the DES solution, the only physical boundary is the nacelle. The axial velocity defect associated to thrust and power generation by the rotor is apparent in top Fig. 10, whereas the radial expansion of the streamtube downstream of the rotor plane is clearly shown by the path of trailing vortices shed by blades. The vertical velocity component in bottom Fig. 10 is consistent with the radial expansion of the turbine wake. In the near wake region characterized by a fine volume grid, the strong velocity perturbations generated by the trailing vortices and the bluff–body wake generated by the nacelle are clearly described. The footprints of blade wakes on the longitudinal plane are hardly visible, as their intensity is very low as compared to tip–vortices. As a consequence of viscous diffusion, the blade wake flow perturbation tends to rapidly disappear at some distance from the rotor plane, whereas tip vortices are coherent structures that persist in the computational domain portion where a sufficient grid refinement exist. At larger distance downstream of the rotor plane, the volume grid is coarse and wake structures are smoothed.

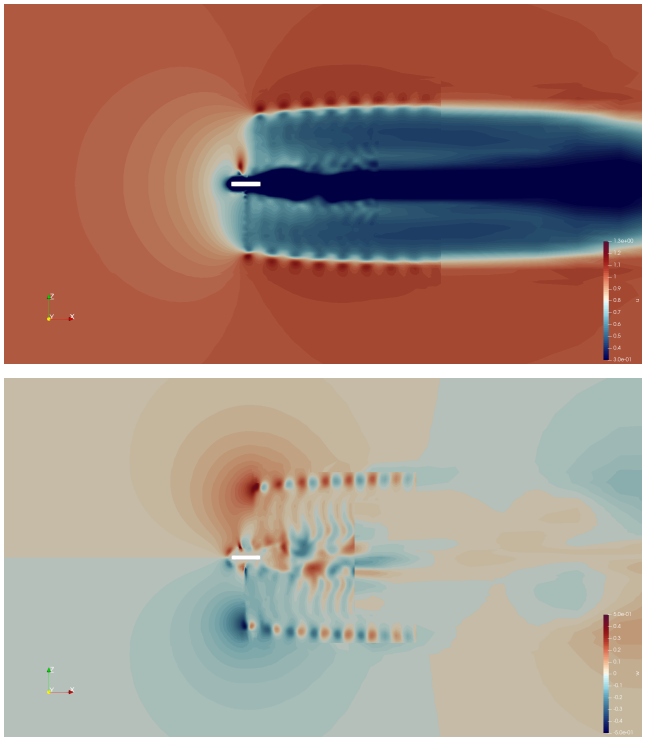

Fig. 10. Turbine in zero inflow turbulence, $\lambda = 5$. Non dimensional axial velocity u_1/V_0 (top) and vertical velocity u_3/V_0 (bottom).

In order to better characterize tip–vortex and hub wake regions, the vorticity field is described in terms of vorticity magnitude $\zeta = \|\nabla \times \mathbf{u}\|$, whereas the so–called λ_2 quantity allows to detect eddies associated to both coherent vortices and turbulence. Following [33], λ_2 is defined as the second eigenvalue of tensor $\Lambda = A^2 + \Omega^2$, where A and Ω represent, respectively, the symmetric and anti–symmetric part of the velocity gradient tensor. A triaxial view of λ_2 iso–surfaces is presented in Fig. 11, with the colormap on the iso–surfaces describing the intensity of the vorticity magnitude. The onset flow is directed from right to left. The footprints of the rotor blades are clearly detected by the vorticity that is generated on these surfaces. In the turbine wake, the vortices shed at blade tips form a regular helicoidal path. The vortical structures released from the boundary layer around the nacelle surface are also visible.

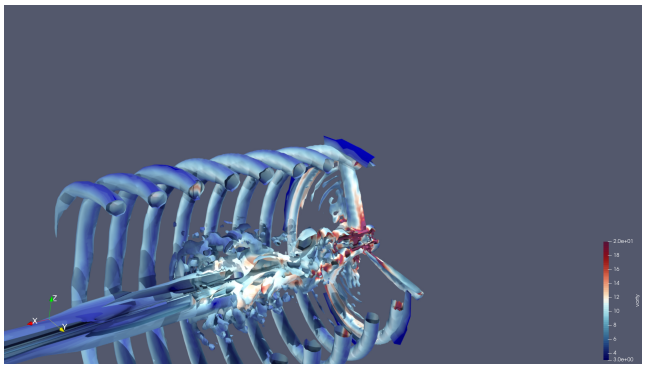

Fig. 11. Turbine in zero inflow turbulence, $\lambda = 5$. λ_2 iso–surfaces with colormap describing the vorticity intensity.

C. Hybrid DES/BIEM analysis in turbulent flow conditions

Numerical results by the hybrid DES/BIEM model with turbulence generation are presented in this section. A 16% turbulence intensity ($I_0 = 0.16$) is imposed as the target condition, and the turbine operating condition is identical to the case discussed in the previous section, $\lambda = 5$. During the time–marching solution, the flow perturbation associated to turbulence generation expands in the computational domain with an averaged convection speed approximately corresponding to the onset flow speed V_0. Downstream of the turbulence generation region, the flow is characterized by significant fluctuations of flow variables as the effect of turbulent eddies that are continuously generated with random distribution in time and space, as described in section II.

Figure 12 presents the distribution of non dimensional axial velocity u_1/V_0 and vertical velocity u_3/V_0 in the longitudinal plane $x_2 = 0$. The flow is directed left to right, and the plotted flowfields can be compared with those in Fig. 10 for the zero inflow turbulence case. Due to the unified volume force approach used, both the turbulence generation obstacle and the rotor blades are visible in the computational domain only through the perturbation they induce to the flow. The contourmaps illustrate how the turbulence injected in the onset flow interacts with the vorticity pattern in the turbine wake. In order to capture this phenomenology in the numerical solution, a fine grid is required. Figure 12 reveals that this condition is satisfied only in the region between the generation and the rotor disc and partially downstream of the rotor disc. This region corresponds to the control grid block shown in Fig. (3).

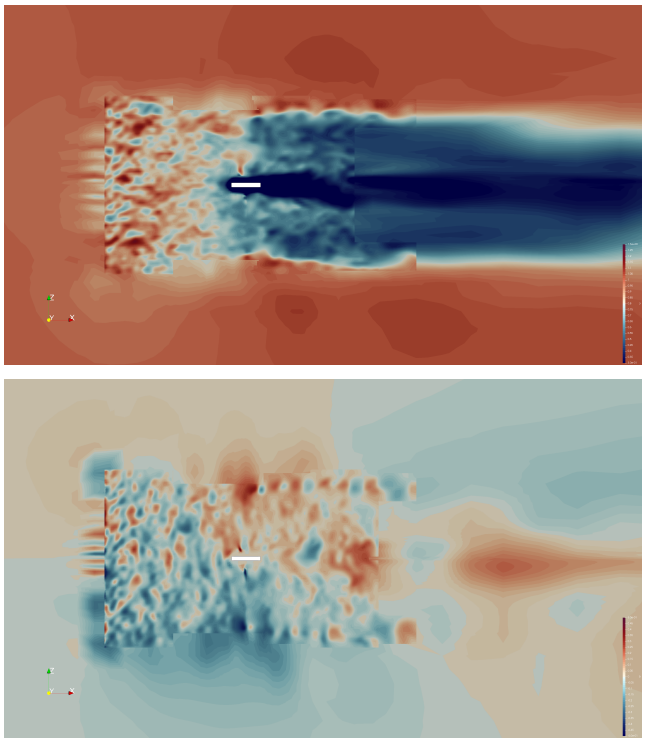

Fig. 12. Turbine in 16% turbulent flow, $\lambda = 5$: non dimensional axial velocity u_1/V_0 (top) and vertical velocity u_3/V_0 (bottom).

In addition to eddies in the incoming flow, another major difference with respect to the zero inflow turbulence case, is the velocity defect associated with the turbulence generation block in the fluid domain. This aspect is well known in experimental tests where physical grids are used to generate turbulence [22]. With reference to the present computational model, the problem is addressed in [18], where the results of unbounded flow simulations with increasing levels of target turbulence intensity, from 10% to 30% are presented. In particular, in the $I_\infty = 0.10$ case, the averaged axial velocity at distance $2D$ downstream of the generation block was found equal to 96.8% of the nominal freestream velocity, whereas it reduced to 82.2% and 75.4%, respectively, with 20% and 30% turbulence intensity.

In order to determine the mean velocity and other statistical properties of the turbulent flow upstream and downstream of the turbine, the control grid block defined in Fig. (3) is splitted along the x_1 direction into four identical sub–blocks, see Fig. 13. The sub–blocks are numbered 1 to 4 moving from upstream (right) to downstream (left) and sub–blocks centers are identified as probes P_1 to P_4. The turbulence generation block is placed upstream of the sub–block 1, whereas the turbine is positioned between the second and third sub–blocks. Table IV presents results for spatial mean velocity components $\overline{u_i}$ and variance $\overline{\sigma}_i^2$, obtained by

averaging quantities at each grid cell in sub–blocks 1 and 2. Spatial means are compared with time mean velocity components $\tilde{u_i}$ and variance $\tilde{\sigma}_i^2$, obtained by averaging time series at sub–blocks probes P_1 and P_2. Data are representative of a time step when the time–marching solution reaches a regime condition.

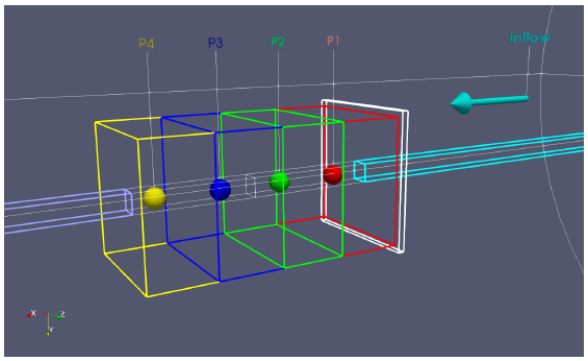

Fig. 13. Near–field region of the computational domain with generator grid block and control grid block splitted into four sub–blocks.

TABLE IV
NORMALIZED SPATIAL AND TIME MEANS OF VELOCITY AND VARIANCE UPSTREAM OF THE TURBINE.

Sub-block 1	$i=1$	$i=2$	$i=3$
$\overline{u}_i/V_0$	0.900	-.0361	-.0362
$\tilde{u}_i/V_0$	0.891	-.0463	-.0333
$\overline{\sigma}_i^2/V_0^2$	0.0181	0.0157	0.0160
$\tilde{\sigma}_i^2/V_0^2$	0.0205	0.0163	0.0198

Sub-block 2	$i=1$	$i=2$	$i=3$
$\overline{u}_i/V_0$	0.852	-.0290	-.0291
$\tilde{u}_i/V_0$	0.786	-.0358	-.0369
$\overline{\sigma}_i^2/V_0^2$	0.0121	0.0097	0.0098
$\tilde{\sigma}_i^2/V_0^2$	0.0086	0.0063	0.0064

By using the results in Table IV, and the relationship between turbulence intensity and variance in (7), one obtains that in sub–block 1 the turbulence intensity calculated by the spatial mean variance is $I_\infty^{s,1} = .129$, and calculated by time mean variance at probe 1 is $I_\infty^{p,1} = .137$. This corresponds to turbulence levels that are, respectively, 19.3% and 14.4% lower than the target value $I_0 = 0.16$. Variance data from sub–block 1 are taken as input in the control strategy described in section II-B. The above results reveal that the PID–based algorithm allows to obtain only a qualitative matching of requested conditions. Moving downstream to the sub–block 2 region, turbulence intensity reduces under the effect of numerical dissipation and of the interaction with the turbine–induced perturbation that reduces the actual flow speed, as apparent from $\overline{u}_i, \tilde{u}_i$ values in the table. The spatial mean gives $I_\infty^{s,2} = .103$, whereas the time mean at probe P_2 yields $I_\infty^{p,2} = .084$. Quasi identical variance terms are obtained in the x_2, x_3 directions, and slightly higher values in the streamwise direction x_1. It can be concluded that a non-homogeneous, approximately isotropic field is generated. A quantitative analysis of turbulent flow isotropy is also presented later.

Results in Table IV describe the properties of the *total* velocity field from the hybrid DES/BIEM solution. In order to characterize the turbine performance, it is important to consider the *effective* velocity calculated by subtracting the turbine–induced perturbation by BIEM from the total velocity distribution in the hybrid DES/BIEM solution. In this case, by a calculation not shown here, a mean effective axial velocity component $V_{eq} = 0.93V_0$ is found. As expected, this value is higher than the $\overline{u_1}$ component in Table IV, as effect of the turbine perturbation that decelerates the flow. Moreover, the found V_{eq} value is in agreement with mean velocity results obtained in [18] where an equivalent computational grid was used for the turbulent flow simulation with no turbine perturbation.

The 7% defect of the axial velocity incoming to the turbine is primarily responsible for a variation of turbine blade loading as compared with the zero inflow turbulence case. Figure 14 presents the time history of turbine thrust and power coefficients predicted by BIEM for the 16% and zero inflow turbulence conditions. Results are normalized with respect to the mean values C_{T0} and C_{P0} at convergence of the zero inflow turbulence case. The turbulent front generated from computation start, takes about 220 time steps to reach the turbine region. The occurrence of thrust and power fluctuations as the turbulent flow impinges on the turbine blades is apparent. A reduction of both C_T and C_P mean values with respect to the zero inflow turbulence case is observed, due to the lower intensity of the effective inflow speed V_{eq} as described above. Figure 14 also presents modified thrust and power coefficients calculated by replacing the nominal inflow speed V_0 with the effective velocity V_{eq} in the non dimensional expressions given by Eq. (11).

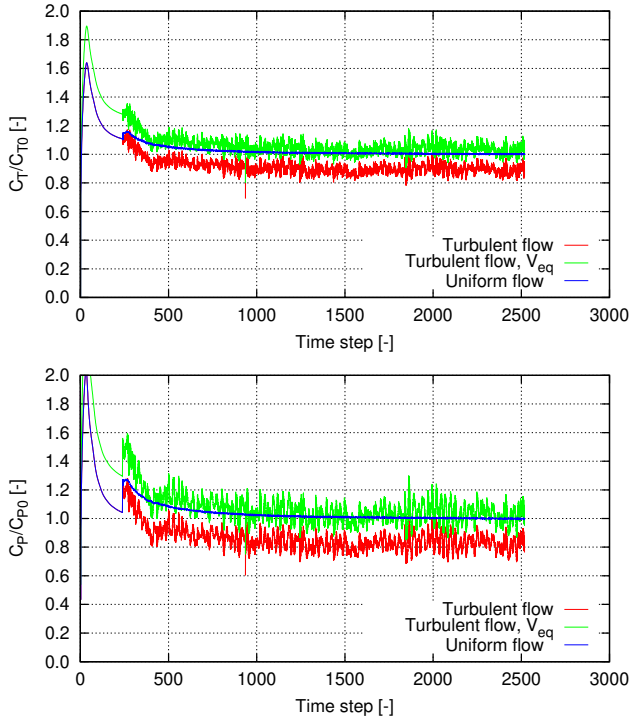

Fig. 14. Turbine in 16% turbulent flow, $\lambda = 5$. Time history of turbine loads predicted by BIEM and comparison with results in the zero inflow turbulence conditions. Top: thrust coefficient; Bottom: power coefficient. Normalized data with respect to mean values C_{T0} and C_{P0} in the zero inflow turbulence case.

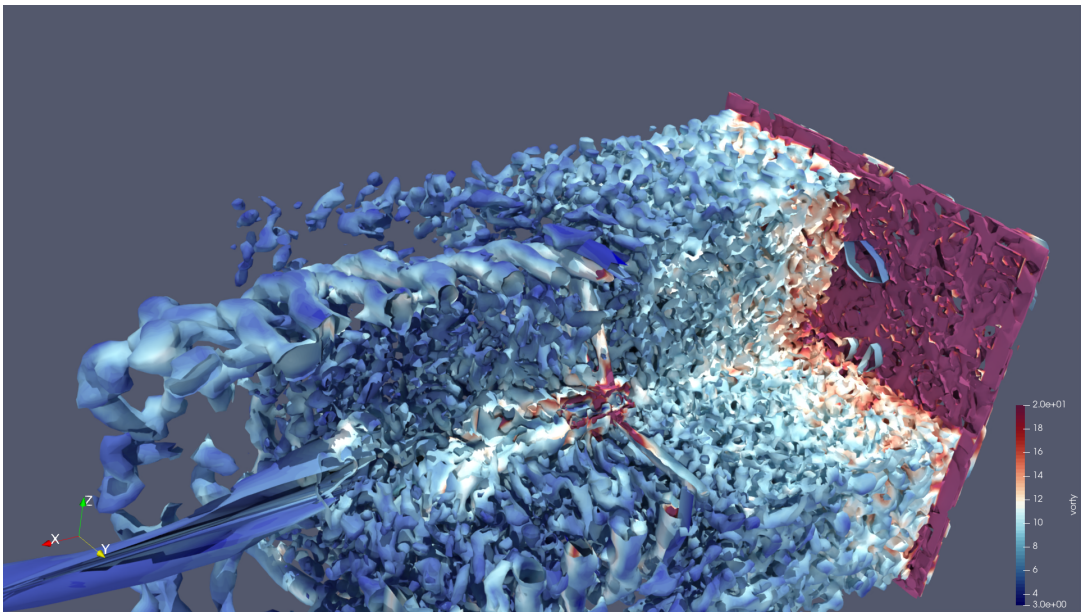

Fig. 15. Turbine in 16% turbulent flow, $\lambda = 5$: the λ_2 iso–surface colormap describes the vorticity intensity at a representative time step.

It is interesting to observe that modified thrust and power coefficients fluctuate around mean values that are very close to those obtained under zero inflow turbulence conditions. Specifically, in the turbulent case thrust and power fluctuations are within, respectively, 15% and 25% of uniform flow values, whereas mean thrust and power are, respectively, 2% and 3% higher than in uniform flow conditions. This would confirm a well known result from experimental as well as CFD studies that onset flow turbulence may have a significant impact on turbine loading fluctuations whereas averaged values are marginally affected. However, the BIEM solver has a limited capability to describe the complex phenomenology of the impact of turbulent eddies on the surface of blades, and hence present results should be taken as a qualitative information.

Figure 15 depicts the λ_2 iso–surfaces with colormaps representing the intensity of magnitude vorticity. The mapped fluid region corresponds to the turbulence generation block (on the right) and the turbulence control block (Fig. 3) with a quarter portion removed to show the flow inside the block. This flow visualization can be compared with the corresponding one in the zero inflow turbulence case, Fig 11. The turbulence generation region is clearly identified by strong vorticity levels whose intensity rapidly reduces as the eddies are convected downstream. In the rotor plane region, the footprints of two of the three blades are visible, whereas the third blade is hidden by the structures in the flow. Comparing the 16% and zero turbulence flow fields, the impact of incoming eddies on the turbine trailing vorticity pattern is apparent. In particular, the regular helicoidal tip vortex path in the zero turbulence case is corrupted under the interaction with eddies in the flow.

A direct comparison between solutions with zero and 16% turbulence intensity in the flow incoming to the turbine is presented in Fig. 16, where the distribution of the λ_2 quantity along the longitudinal plane $x_2 = 0$ for a representative time step is plotted. The turbulent flow case is in the top half plane, and the zero–turbulence flow case is in the bottom half plane. The edges of main grid blocks are shown (see Fig. 3). The flow is directed left to right. On the left side, the turbulence generation block is clearly identified with a thin vertical layer where eddies are generated. The intensity of structures reduces between the first and the second partition of the control block. The turbine position is identified by the nacelle surface and by the rotor grid block where the volume forces simulating blade loads are distributed. Tip vortices are shed at the downstream edge of the rotor grid block, and in the zero turbulence case evolve into a regular path of coherent structures. A quite different phenomenology can be observed in the turbulent flow case, where the tip vortex path is rapidly distorted, as argued from Fig 15 above. Furthermore, vortex cores are smeared into relatively large regions with lack of regularity of the axial spacing among each other. Similar effects are observed in the nacelle wake. This is an effect of the interaction with turbulent eddies in the flow, with higher vorticity diffusion and viscous dissipation than in the smooth, zero turbulence flow case. The differences in the wakefield are apparent also in Fig. 17, where normal planes at the rotor plane $x_1 = 0$, and downstream of it, $x_1 = 0.5D$ and $x_1 = D$ are plotted. The zero–turbulence case is on the left side and the 16% turbulence case on the right side. From these views, the loss of coherence of the tip vortices is apparent. In particular, moving from the rotor plane to downstream, the eddies entrained into the streamtube are attracted towards the tip–vortex region and towards the nacelle wake, as effect of the velocity induced by vortices shed at blade tip and root.

A quantitative comparison of velocity intensity in the turbine wake for the zero and 16% turbulence cases is presented in Fig. 18, where the non–dimensional axial component u_1/V_0 and vertical component u_3/V_0 for

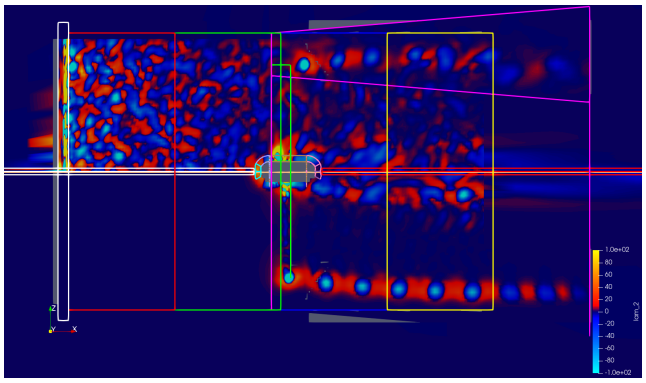

Fig. 16. Turbine wake flow, $\lambda = 5$. λ_2 distribution in the longitudinal plane $x_2 = 0$. Solution with $I_\infty = 0.16$ turbulent flow (top half plane) and in the zero–turbulence case (bottom half plane).

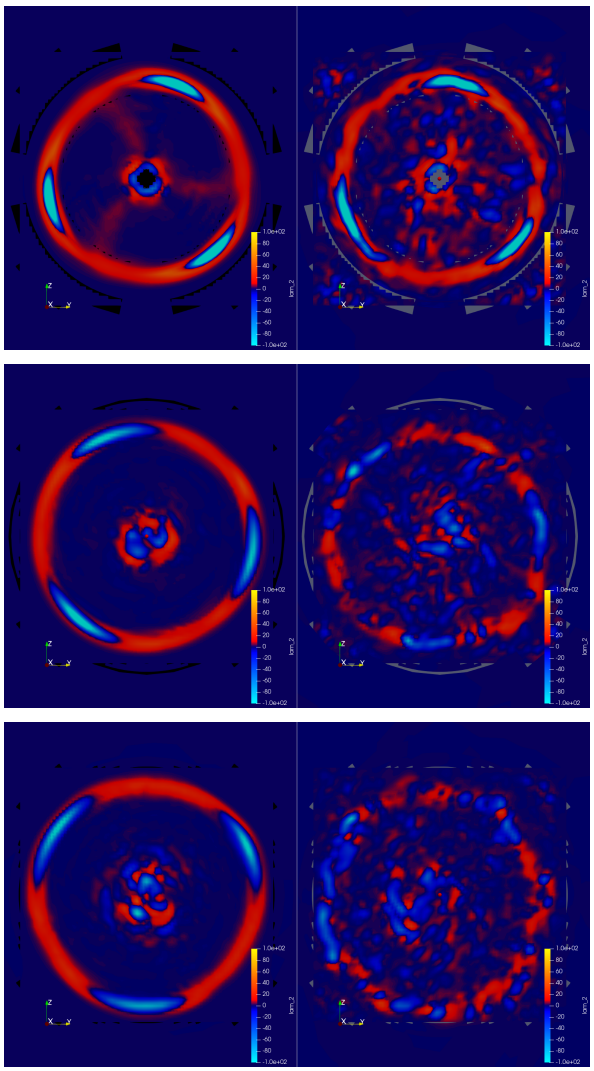

Fig. 17. Turbine wake flow, $\lambda = 5$. λ_2 distribution in normal plane at constant x_1. Solution with $I_\infty = 0.16$ turbulent flow (right) and in the zero–turbulence case (left). Top to bottom: $x_1/D = 0, 0.5, 1$.

constant radius positions $r/R = 0.7, 1.0, 1.1$ between $x_1 = 0$ (rotor plane), and $x_1 = 1.7D$ are plotted. The oscillations of the velocity intensity (notably, the radial component) confirm the regularity of the tip–vortex path in the zero turbulence case that in the 16% turbulence case, is broken under the effect of the travelling eddies.

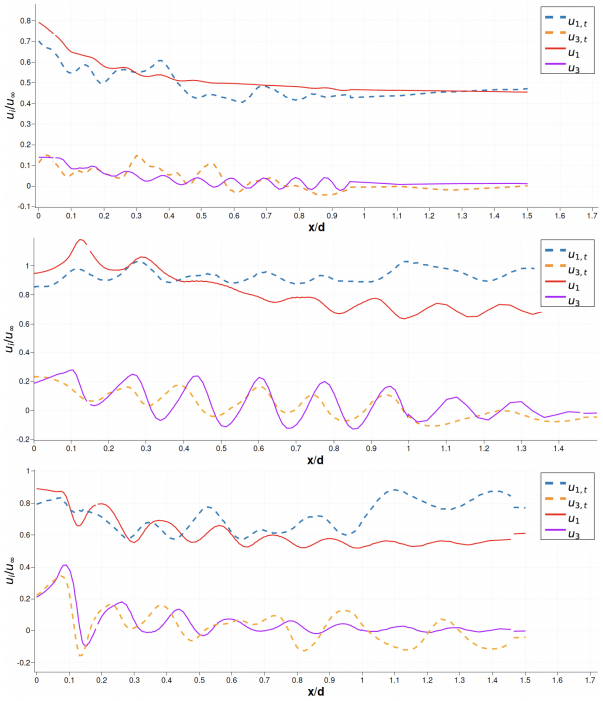

Fig. 18. Turbine wake flow, $\lambda = 5$. Non–dimensional axial velocity u_1/V_∞ and vertical velocity u_3/V_∞ at radial positions $r/R = 0.7, 1.0, 1.1$ (top to bottom). Results for $I_\infty = 0.16$ and zero–turbulence cases compared.

The description of the flow field including turbulence generation and turbine–induced perturbation is completed by analyzing the divergence of the velocity field. Figure 19 shows the non–dimensional divergence $\nabla \cdot \mathbf{u}$ at a representative time step at control block points at $x_2 = x_3 = 0$. Pointwise values are averaged over a 5×5 grid cell stencil. The largest values are observed in the region between the generation block and the rotor block, with a peak value of 0.014 at the rotor plane position $x_1 = 0$. In the other flow regions, relatively small values are obtain, and it can be concluded that the divergence–free condition is fairly satisfied in the numerical solution.

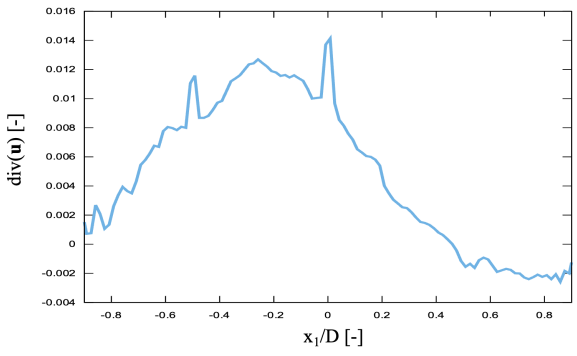

Fig. 19. Turbine wake flow, $\lambda = 5$. Non–dimensional divergence of the velocity field at representative time step and control block points at $x_2 = x_3 = 0$.

D. Turbulence metric analysis

In this section, some results of a statistical analysis on the calculated velocity field are presented. In particular, key turbulence metric quantities are evaluated with

respect to the four sub–blocks in which the control grid block is splitted, as shown in Fig. 13. Recalling a hybrid DES/BIEM model is used, the perturbation induced by the turbine in sub–blocks 1 and 2 presents an irrotational flow nature, with pressure increase and flow deceleration as the distance from the rotor disc reduces. A completely different phenomenology is expected in sub–blocks 3 and 4 downstream of the rotor disc, where vortical structures and shear layers generated on blade and nacelle surfaces are shed into the wake.

Power Spectral Density (PSD) distributions are presented to analyse the physical consistency of the calculated turbulent flow. Results for the PSD at probes P_1 to P_4 are presented in Fig. 20 where the Kolmogorov $k^{-5/3}$ law is plotted as reference. At probes P_1 and P_2, the spectrum follows a white noise behaviour in the low frequency range. This can be explained recalling the onset flow turbulence is generated at relatively small distance from these probes by forcing terms with stocastic intensity and distribution, as described in section II. In this region, a kinetic energy decay with a $-5/3$ slope is found only in a very narrow range around 10 Hz. A much wider region with a $-5/3$ slope in the sub–inertial frequency range is observed at probes P_3 and P_4 that fall within the nacelle wake, where the onset flow structures interact with the turbulence generated by the nacelle boundary layer.

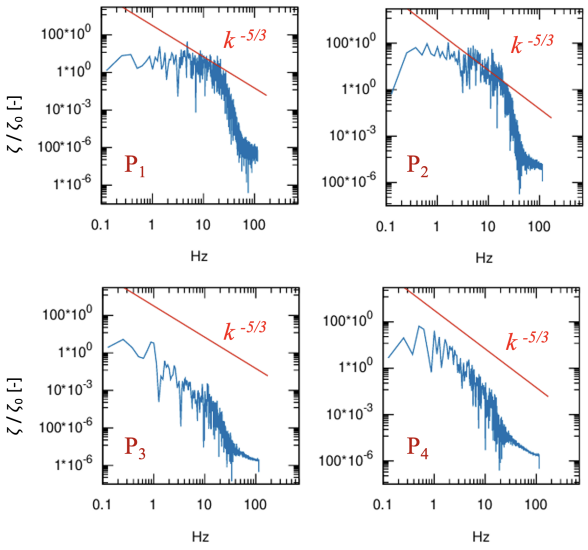

Fig. 20. Turbine in 16% turbulent flow, $\lambda = 5$. Kinetic energy Power Spectral Density (PSD) at probes P_i with $i = 1$ to 4, left to right, top to bottom.

Finally, the isotropy of the velocity field is analysed. Following [23] and [34], the invariants of the tensor $\mathbf{S}$ related to the correlation tensor $\mathbf{R}$ by the expression $S_{ij} = R_{ij}(0) - 1/3 R_{ii}(0)\delta_{ij}$ are considered. In particular, the isotropy of a random signal can be investigated by considering the second and third invariant, respectively, $\mathbf{II} = 1/2[(S_{ii})^2 - S_{ii}^2]$ and $\mathbf{III} = det(\mathbf{S})$. By mapping events in the $(\mathbf{II}, \mathbf{III})$ plane, a perfectly isotropic signal is characterized by $\mathbf{II} = 0$ and $\mathbf{III} = 0$. Figure 21 presents the results of this analysis by considering flow conditions at the four probes P_i for 20 representative time steps after the turbulent front has crossed the near wake region represented by sub–blocks 3 and 4 in Fig. 13. The time steps are indicated by the different colors. The two curves converging to the origin of the $(\mathbf{II}, \mathbf{III})$ plane delimit the feasible region. Moving from probe P_1 to P_2, the onset turbulent flow tends to isotropy, whereas this condition is broken donwstream of the rotor plane, at probes P_3 and P_4 that are immersed into the nacelle wake. In particular, just downstream of the nacelle tail (probe P_3), the phenomenology is typical of a Log–law flow region associated to the nacelle boundary layer [34], whereas moving to probe P_4 a trend to partially recover an isotropic behaviour is noted.

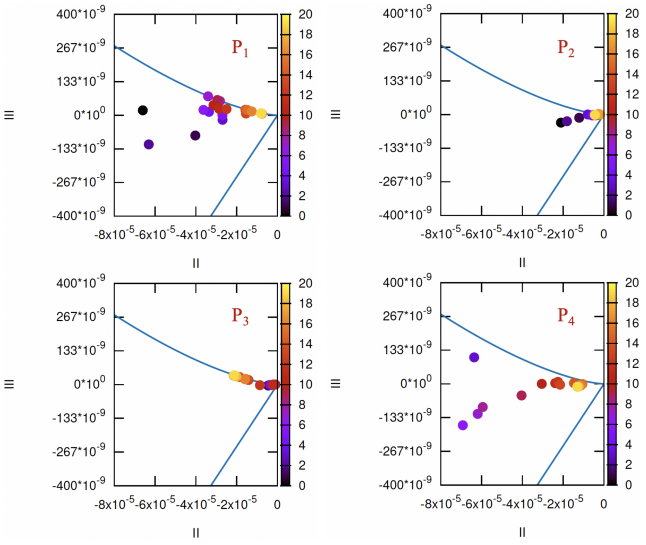

Fig. 21. Turbine in 16% turbulent flow, $\lambda = 5$. Isotropy diagrams by using S_{ij} tensor invariants $\mathbf{II}, \mathbf{III}$ from [34]. Top to bottom, left to right: probes 1 to 4. The colormap marks samples at increasing time steps.

VI. Conclusions

A computational methodology to simulate the operation of hydrokinetic turbines in turbulent onset flows has been presented. The turbulence is generated by a random distribution of volume force terms in the right–hand side of the Navier–Stokes equations. A control strategy is used to enforce that the perturbation determines flow conditions that are representative of prescribed turbulent flow conditions. The numerical solution of the Navier–Stokes equations is obtained by a hybrid viscous/inviscid formulation in which a Boundary Integral Equation Method (BIEM) is used to predict the perturbation induced by a turbine, whereas the surrounding viscous flow is described by Detached Eddy Simulation (DES). BIEM and DES solvers are strongly coupled with turbine blade loading by BIEM recast as volume forces in the DES solver.

The results of a numerical application describing a horizontal–axis turbine in a 16% turbulent onset flow have been discussed. In spite of the limited scope of the study, with only one turbine operating condition addressed, the analysis allows to draw some conclusions. Downstream of the generation region, the turbulent stream tends to achieve isotropy conditions, with a turbulence intensity 19% lower than the imposed value.

A better agreement could be obtained by adopting a more sophisticated control strategy than the simple PID used in the present analysis. The volume force distribution imposed to generate turbulence in the flow behaves like a physical obstacle and determines a velocity defect downstream of the generation region. In the present case, a 6.7% reduction of the axial velocity incoming to the turbine plane has been measured. This results into lower turbine thrust and power than in zero turbulence conditions. The interaction between blades and incoming eddies determines thrust and power fluctuations that are, respectively, 15% and 25% of the corresponding values in zero turbulence conditions. As expected, if thrust and power coefficients are scaled with respect to the actual inflow speed, their mean values are very close to those calculated in zero turbulence conditions. The analysis of the Power Spectral Density has shown that the kinetic energy spectrum is largely affected by the definition of the random distribution of the turbulence generation forcing terms. However, in the turbine wake, the interaction among incoming eddies and turbine–generated structures tends to establish conditions that are representative of real turbulent flows. Another important finding is that the calculated flow field including turbulence generation and turbine–induced perturbation fairly satisfies the divergence–free condition for incompressible flows.

Ongoing work is dedicated to investigate the effects of numerical aspects like the computational grid refinement, and the definition of turbulence generation forcing terms. The simulation of a range of turbine operating conditions is also in progress. The objective is to assess the capability of the proposed methodology as an engineering tool that can be used to predict the performance of single turbines and arrays in the turbulent flow climates of real tidal sites.

ACKNOWLEDGEMENTS

The authors are grateful to profs. Grégory Pinon at Le Havre Normandie University, and Gianpaolo Romano at Rome Sapienza University, for their valuable review of Dr. Gregori's PhD thesis where the present methodology has been developed. Dr. Roberto Muscari at CNR-INM is also acknowledged for his constant support with the DES model.

REFERENCES

[1] T. Blackmore, L. E. Myers, and A. S. Bahaj, "Effects of turbulence on tidal turbines: Implications to performance, blade loads, and condition monitoring," *International Journal of Marine Energy*, vol. 14, pp. 1–26, 2016. [Online]. Available: https://www.sciencedirect.com/science/article/pii/S2214166916300297

[2] I. Milne, A. Day, R. Sharma, and R. Flay, "The characterisation of the hydrodynamic loads on tidal turbines due to turbulence," *Renewable and Sustainable Energy Reviews*, vol. 56, pp. 851–864, 2016. [Online]. Available: https://www.sciencedirect.com/science/article/pii/S1364032115013623

[3] M. Thiébaut, J.-F. Filipot, C. Maisondieu, G. Damblans, R. Duarte, E. Droniou, N. Chaplain, and S. Guillou, "A comprehensive assessment of turbulence at a tidal-stream energy site influenced by wind-generated ocean waves," *Energy*, vol. 191, p. 116550, 2020. [Online]. Available: https://www.sciencedirect.com/science/article/pii/S0360544219322455

[4] I. A. Milne, R. N. Sharma, R. G. J. Flay, and S. Bickerton, "Characteristics of the turbulence in the flow at a tidal stream power site," *Philosophical Transactions of the Royal Society A: Mathematical, Physical and Engineering Sciences*, vol. 371, no. 1985, p. 20120196, 2013. [Online]. Available: https://royalsocietypublishing.org/doi/abs/10.1098/rsta.2012.0196

[5] B. G. Sellar, G. Wakelam, D. R. J. Sutherland, D. M. Ingram, and V. Venugopal, "Characterisation of tidal flows at the european marine energy centre in the absence of ocean waves," *Energies*, vol. 11, no. 1, 2018. [Online]. Available: https://www.mdpi.com/1996-1073/11/1/176

[6] P. Mycek, B. Gaurier, G. Germain, G. Pinon, and E. Rivoalen, "Experimental study of the turbulence intensity effects on marine current turbines behaviour. part i: One single turbine," *Renewable Energy*, vol. 66, pp. 729–746, 2014. [Online]. Available: https://www.sciencedirect.com/science/article/pii/S096014811400007X

[7] ——, "Experimental study of the turbulence intensity effects on marine current turbines behaviour. part ii: two interacting turbines," *Renewable Energy*, vol. 68, pp. 876–892, 2014. [Online]. Available: https://www.sciencedirect.com/science/article/pii/S096014811400007X

[8] R. S. Rogallo and P. Moin, "Numerical simulation of turbulent flows," *Annual Review of Fluid Mechanics*, vol. 16, no. 1, pp. 99–137, 1984. [Online]. Available: https://doi.org/10.1146/annurev.fl.16.010184.000531

[9] X. Wu, "Inflow turbulence generation methods," *Annual Review of Fluid Mechanics*, vol. 49, no. 1, pp. 23–49, 2017. [Online]. Available: https://doi.org/10.1146/annurev-fluid-010816-060322

[10] T. S. Lund, X. Wu, and K. D. Squires, "Generation of turbulent inflow data for spatially-developing boundary layer simulations," *Journal of Computational Physics*, vol. 140, no. 2, pp. 233–258, 1998. [Online]. Available: https://www.sciencedirect.com/science/article/pii/S002199919895882X

[11] M. C. Adler, D. R. Gonzalez, C. M. Stack, and D. V. Gaitonde, "Synthetic generation of equilibrium boundary layer turbulence from modeled statistics," *Computers & Fluids*, vol. 165, pp. 127–143, 2018. [Online]. Available: https://www.sciencedirect.com/science/article/pii/S0045793018300033

[12] R.-E. Keck, R. Mikkelsen, N. Troldborg, M. de Maré, and K. S. Hansen, "Synthetic atmospheric turbulence and wind shear in large eddy simulations of wind turbine wakes," *Wind Energy*, vol. 17, no. 8, pp. 1247–1267, 2014. [Online]. Available: https://onlinelibrary.wiley.com/doi/abs/10.1002/we.1631

[13] G. Tabor and M. Baba-Ahmadi, "Inlet conditions for large eddy simulation: A review," *Computers and Fluids*, vol. 39, no. 4, pp. 553–567, 2010. [Online]. Available: https://www.sciencedirect.com/science/article/pii/S0045793009001601

[14] C. Choma Bex, C. Carlier, A. Fur, G. Pinon, G. Germain, and Élie Rivoalen, "A stochastic method to account for the ambient turbulence in lagrangian vortex computations," *Applied Mathematical Modelling*, vol. 88, pp. 38–54, 2020. [Online]. Available: https://www.sciencedirect.com/science/article/pii/S0307904X20302614

[15] N. J. Mullenix, D. V. Gaitonde, and M. R. Visbal, "Spatially developing supersonic turbulent boundary layer with a body-force-based method," *AIAA Journal*, vol. 51, no. 8, pp. 1805–1819, 2013.

[16] F. Houtin-Mongrolle, L. Bricteux, P. Benard, G. Lartigue, V. Moureau, and J. Reveillon, "Actuator line method applied to grid turbulence generation for large-eddy simulations," *Journal of Turbulence*, vol. 21, no. 8, pp. 407–433, 2020. [Online]. Available: https://doi.org/10.1080/14685248.2020.1803495

[17] M. Togneri, G. Pinon, C. Carlier, C. Choma Bex, and I. Masters, "Comparison of synthetic turbulence approaches for blade element momentum theory prediction of tidal turbine performance and loads," *Renewable Energy*, vol. 145, pp. 408–418, Jan. 2020. [Online]. Available: https://hal-normandie-univ.archives-ouvertes.fr/hal-03388939

[18] M. Gregori, F. Salvatore, and R. Camussi, "Turbulent eddy generation for the cfd analysis of hydrokinetic turbines," *Journal of Marine Science and Engineering*, vol. 10, pp. 1332–1356, 2022. [Online]. Available: https://www.mdpi.com/2077-1312/10/10/1332

[19] R. Muscari, R. Broglia, and A. Di Mascio, "An overlapping grids approach for moving bodies problem," in *16^{th} Int. Offshore and Polar Engineering Conference, ISOPE 2006, San Francisco, California, USA*, 2011.

[20] F. Salvatore, Z. Sarichloo, and D. Calcagni, "Marine turbine hydrodynamics by a boundary element method with viscous flow correction," *Journal of Marine Science and Engineering*, vol. 6, no. 2, p. 30, 2018. [Online]. Available: https://www.mdpi.com/2077-1312/6/2/53

[21] G. Dubbioso, F. Salvatore, Z. Sarichloo, D. Calcagni, R. Muscari, and R. Starzmann, "Variable-fidelity cfd modelling of horizontal-axis tidal turbines and arrays." in *The Thirteenth European wave and Tidal Energy Conference*, 2019.
[22] S. Weitemeyer, N. Reinke, J. Peinke, and M. Hölling, "Multi-scale generation of turbulence with fractal grids and an active grid," *Fluid Dynamics Research*, vol. 45, no. 6, p. 061407, aug 2013. [Online]. Available: https://doi.org/10.1088/0169-5983/45/6/061407
[23] S. B. Pope, *Turbulent Flows*. Cambridge university Press, 2000.
[24] F. Salvatore, D. Calcagni, and Z. Sarichloo, "Development of a viscous/inviscid hydrodynamics model for single turbines and arrays," in *Proc. EWTEC'17, Twelfth European wave and Tidal Energy Conference*, 2017.
[25] R. Muscari, G. A. Dubbioso, and A. Di Mascio, "Analysis of the flow field around a rudder in the wake of a simplified marine propeller," *Journal of Fluid Mechanics*, vol. 814, pp. 547–569, 2017.
[26] L. Morino, "Boundary integral equations in aerodynamics," *Applied Mechanics Reviews*, vol. 46, no. 8, pp. 445–466, 1993.
[27] M. Drela, "Xfoil: An analysis and design system for low reynolds number airfoils," in *Low Reynolds number aerodynamics*. Springer, 1989, pp. 1–12.
[28] P. R. Spalart, "Detached-eddy simulation," *Annual Review of Fluid Mechanics*, vol. 41, pp. 181–202, 2009.
[29] C. Merkle and M. Athvale, "Time-accurate unsteady compressible flow algorithms based on artificial compressibility," in *The 8th Computational Fluid Dynamics AIAA Conference, Honolulu, HI, USA*, vol. AIAA Paper 87-1137, 1987, pp. 397–407.
[30] R. Starzmann, I. Goebel, and P. Jeffcoate, "Field performance testing of a floating tidal energy platform–part i: Power performance," in *The Asian wave and Tidal Energy Conference, Taiwan*, 2018.
[31] Z. Sarichloo, F. Salvatore, F. Di Felice, M. Costanzo, R. Starzmann, and C. Frost, "Computational analysis and experimental verification of a boundary integral equation model for tidal turbines," in *Advances in Renewable Energies Offshore: Proceedings of the 3rd International Conference on Renewable Energies Offshore (RENEW 2018), October 8-10, 2018, Lisbon, Portugal*. CRC Press, 2018, p. 209.
[32] D. Calcagni, F. Salvatore, G. Dubbioso, and R. Muscari, "A generalised unsteady hybrid des/bem methodology applied to propeller–rudder flow simulations," in *Seventh International Conference on Computational Methods in Marine Engineering (MARINE), Nantes, France*, 2017.
[33] J. Jeong and F. Hussain, "On the identification of a vortex," *Journal of Fluid Mechanics*, vol. 285, p. 69–94, 1995.
[34] K.-S. Choi and J. L. Lumley, "The return to isotropy of homogeneous turbulence," *Journal of Fluid Mechanics*, vol. 436, p. 59–84, 2001.